01 Mar 2020

A Molecular Dynamics Study of Transient Evaporation and Condensation

Zhi Liang
Missouri University of Science and Technology, zlch5@mst.edu

Anirban Chandra

Eric Bird

Pawel Keblinski

Recommended Citation

Z. Liang et al., "A Molecular Dynamics Study of Transient Evaporation and Condensation," *International Journal of Heat and Mass Transfer*, vol. 149, article no. 119152, Elsevier, Mar 2020.
The definitive version is available at https://doi.org/10.1016/j.ijheatmasstransfer.2019.119152

International Journal of Heat and Mass Transfer 149 (2020) 119152

Contents lists available at ScienceDirect

International Journal of Heat and Mass Transfer

journal homepage: www.elsevier.com/locate/hmt

A molecular dynamics study of transient evaporation and condensation

Zhi Liang[a,*], Anirban Chandra[c], Eric Bird[a], Pawel Keblinski[b,*]

[a] Department of Mechanical Engineering, California State University, Fresno, CA 93740, USA
[b] Department of Materials Science and Engineering, Rensselaer Polytechnic Institute, Troy, N.Y. 12180, USA
[c] Department of Mechanical, Aerospace, and Nuclear Engineering, Rensselaer Polytechnic Institute, Troy, N.Y. 12180, USA

ARTICLE INFO

Article history:
Received 11 April 2019
Revised 18 November 2019
Accepted 30 November 2019
Available online 13 January 2020

Keywords:
Molecular dynamics
Transient evaporation and condensation
Schrage relationships

ABSTRACT

We use molecular dynamics (MD) simulations to study the transient evaporation and condensation of a pure fluid Ar in a nanochannel. In the MD model, the evaporation and condensation of fluid Ar is initiated by a sudden increase of the temperature or periodically varying the temperature in the solid substrate on one side of the nanochannel. In both cases, we find the transient evaporation and condensation rates obtained directly from MD simulations are in good agreement with the predictions from the Schrage relationships. Furthermore, our analyses show that the kinetics of the transient heat and mass transfer between the evaporating and the condensing surfaces in the nanochannel are mainly controlled by heat and mass diffusion in the vapor rather than by convection. The simulation results indicate that the Schrage relationships are capable of accurately describing the transient evaporation/condensation processes and their rates even under a high-frequency oscillatory driving force condition.

1. Background and introduction

Evaporation and condensation processes are important for various engineering and environmental applications such as spray cooling, spray combustion, and cloud formation [1–5]. A fundamental understanding of the evaporation/condensation at liquid-gas interfaces can be obtained from the kinetic theory of gasses (KTG) [1,6–8]. Hertz and Knudsen derived a relationship between the net evaporation/condensation rate and fluid properties near the liquid-vapor interface based on the KTG more than 100 years ago [6,7]. The Hertz-Knudsen (HK) relationship was later modified by Schrage to take into account the effects of the macroscopic motion of vapor near the evaporating and condensing interface [8]. According to Schrage analysis, the net evaporation molar flux J_{evp} and the net condensation molar flux J_{con} are given by [8]:

$$J_{evp} = \alpha(T_L)\sqrt{\frac{k_B}{2\pi m}}\left(\rho_g(T_L)\sqrt{T_L} - \Gamma(v_R)\rho_v\sqrt{T_v}\right) \tag{1a}$$

$$J_{con} = \alpha(T_L)\sqrt{\frac{k_B}{2\pi m}}\left(\Gamma(-v_R)\rho_v\sqrt{T_v} - \rho_g(T_L)\sqrt{T_L}\right) \tag{1b}$$

where T_L and T_v are the temperature of liquid and vapor near the liquid-vapor interface, respectively, $\rho_g(T_L)$ is the saturated vapor density at T_L, ρ_v is the density of vapor undergoing phase change, k_B is the Boltzmann constant, m is the mass of fluid molecules undergoing phase change, and α is the mass accommodation coefficient (MAC). The MAC is defined as the fraction of vapor molecules that strike the interface and are accommodated to the liquid phase. In Eq. (1) the effects of macroscopic vapor motion are taken into account by the function $\Gamma(v_R)$ which is given by

$$\Gamma(v_R) = e^{-v_R^2} - v_R\sqrt{\pi}[1 - erf(v_R)]. \tag{2}$$

where v_R is the ratio of the macroscopic speed of vapor, $v_{v,0}$, to the most probable thermal speed of vapor molecules,

$$v_R = \frac{v_{v,0}}{\sqrt{2k_BT_v/m}}. \tag{3}$$

The only difference between the HK relationships and the Schrage relationships (i.e. Eq. (1)) is that the HK relationships assume zero mean velocity in vapor (i.e. $v_{v,0} = 0$), which makes $\Gamma(v_R)$ in Eq. (2) equal to 1 [6,7]. Eqs. (1a) and (1b) are implicit equations for J_{evp} and J_{con}. One needs to use the iterative procedure to find J_{evp} and J_{con} from Eq. (1) [9].

Although the Schrage relationships have been used for many decades, their accuracy and even validity has never been truly verified by experiment. The experimental quantification of evaporation and condensation processes requires a local measurement of fluid temperature and density at a very thin layer near the evaporating and condensing interfaces with sufficient accuracy, which

* Corresponding authors.
E-mail addresses: zliang@csufresno.edu (Z. Liang), keblip@rpi.edu (P. Keblinski).

https://doi.org/10.1016/j.ijheatmasstransfer.2019.119152
0017-9310/

remains challenging [1]. Another challenge in experimental validation of the Schrage relationships is that the kinetic parameter, i.e., MAC, in Eq. (1), cannot be directly determined from experiment [1] and is typically used as a fitting parameter to account properly for the evaporation/condensation rates.

To mitigate the above described experimental challenges, molecular dynamics (MD) simulations have been widely used to conduct numerical experiments in various model fluid systems to study evaporation and condensation processes [9–15]. Using MD simulations, the MAC can be determined accurately based on its definition [9–11]. Therefore, the MAC is not a fitting parameter for accurate predictions of evaporation and condensation rates in our study. Our recent MD study for argon based model fluids [9–11] shows that the Schrage relationships give an accurate description of steady state evaporation and condensation processes and their rates. Under steady conditions, evaporation/condensation flux and all fluid properties in Schrage relationships do not change with time. This greatly simplifies the analysis of evaporation and condensation processes. However, there are often circumstances in which transient evaporation and condensation are critical. For example, the fast evaporation of water droplets has been widely used for the efficient cooling of gas turbines, nuclear reactors, and various electronic devices [1,16,17]. During the fast evaporation process the ambient temperature drops rapidly with time.

Recently, a novel transient experimental study of fast evaporation and condensation was conducted in attempt to investigate an individual liquid-vapor interface [18]. The transient evaporation process is initiated by a picosecond laser pulse heating the solid surface that is in contact with an adsorbed nanoscopic liquid layer. A probe laser pulse is subsequently used to measure changes in the thickness of the liquid layer in response to a fast temperature rise and the subsequent thermal relaxation process that occurs within nanoseconds [18]. While such an experiment is a significant advance toward the quantification of the transient evaporation/condensation processes, determination of the MAC requires knowledge of the proper theoretical model. In this context, it is not clear e.g., if Hertz-Knudsen or the Schrage relationships are better in the description of the process as the molecular velocity distributions can vary from those assumed either by Hertz and Knudsen or the Schrage due to the transient nature of the process.

In this work, to address the above described gap in our knowledge, we use MD simulations to study the transient evaporation and condensation of fluid Ar in a nanochannel. Using MD simulations coupled with theoretical analyses, we will investigate how accurate the Schrage relationships are in the prediction of the transient evaporation/condensation rates. In the next section, we will describe the model system, simulation details, and vapor transport characteristics. In the third section, we will present results on non-equilibrium molecular dynamics (NEMD) simulations of transient and oscillatory heating. We will finish with a conclusion section.

2. MD simulation of transient evaporation and condensation

2.1. The model system

As depicted in Fig. 1(a), the model system consists of fluid Ar confined by two solid Au slabs. Each Au slab is formed by three (100) oriented Au atomic layers with a cross section area of 38.76 nm by 38.76 nm. We place a 6-nm-thick liquid Ar layer on each of the two inner surfaces of Au slabs. The thickness of the liquid layers in our model is large enough to avoid the effects of disjoining pressure on the equilibrium properties of fluid Ar [9,15]. The distance between the two liquid surfaces is ~106 nm. The left and right boundaries of what we define as the central gas region are ~3 nm away from the left and right liquid surface, respectively, thus resulting in a central gas region length of 100 nm

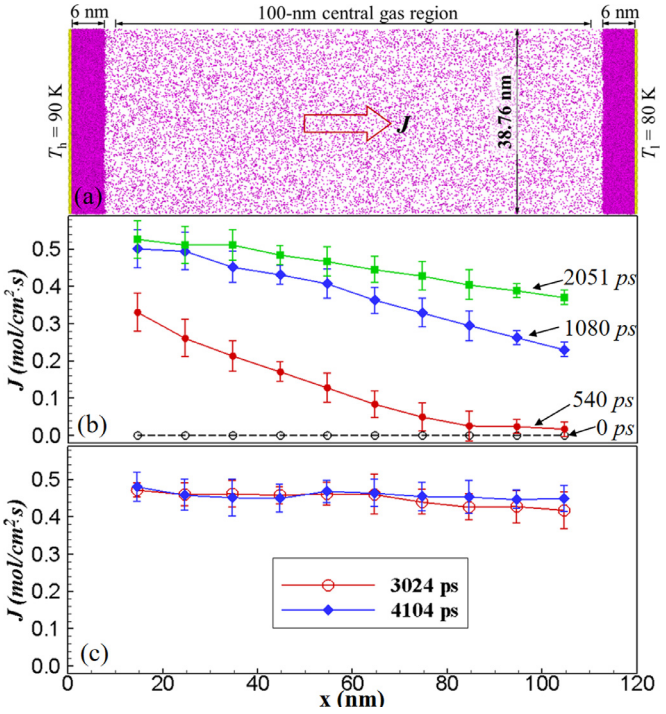

Fig. 1. (a) A snapshot of the model system. The purple and yellow spots represent Ar and Au atoms, respectively. (b) The spatial distribution of molar flux in the central gas region at t = 0 ps, 540 ps, 1080 ps, 2051 ps, and (c) t = 3024 ps, and 4104 ps. The evaporation and condensation are driven by a sudden increase of temperature in the left Au surface. The lines in (b) and (c) are used to guide the reader. (For interpretation of the references to color in this figure legend, the reader is referred to the web version of this article.)

(see Fig. 1(a)). Periodic boundary conditions (PBCs) are applied in the y and z directions, and atoms in the outermost Au layers are fixed in the simulation to prevent shifting of the model system. The total number of Au and Ar atoms in the simulation system is 108,300 and 403,200, respectively.

The embedded-atom-method (EAM) potential [19] is used for Au–Au interactions. The LJ potential with parameters σ= = 3.41 Å and ε= = 10.3 meV [20] is employed for both Ar-Ar and Ar–Au interactions. The cutoff distance for all LJ interactions is 3.2σ. In all MD simulations we use a velocity Verlet algorithm [21] with a time step size of 4 fs to integrate the equations of motions.

2.2. The MD simulation details

The model system is first equilibrated with the Berendsen thermostat [22] at a temperature of 80 K for 6 ns. In the equilibrium process, the model liquid Ar evaporates. After the system reaches the thermal equilibrium, we have the model liquid Ar coexists with its own saturated vapor. Afterwards, we carry out non-equilibrium MD (NEMD) simulations to study the transient evaporation and condensation of fluid Ar in the nanochannel. In NEMD simulations, we keep the temperature of the right Au slab at T_l= = 80 K while we vary the temperature of the left Au slab, T_h, in two ways: (1) suddenly increase T_h from 80 K to 90 K at the beginning of the NEMD simulation and maintain T_h at 90 K for the rest of simulations; (2) vary the temperature of the left Au slab as T_h= = 90 – 10cos(ωt) K, where the angular frequency ω is 2π/(2 ns) and t is time. At each time step of the NEMD simulation, we maintain the temperature of each Au slab by velocity rescaling [23].

To test the accuracy of the Schrage relationships in the prediction of transient evaporation and condensation rates, we calculate the spatial and temporal distributions of molar flux, $J(x,t)$, in the

central gas region and temperature, $T(x,t)$, and density, $\rho(x,t)$, of fluid across the model system. To determine the spatial distribution of temperature and density in liquid, we evenly divide each liquid layer into six bins in the x – direction. The width of each bin in liquid is 1 nm. In the course of transient evaporation and condensation in this study, the position of the liquid surface is shifted by less than 0.5 nm. Therefore, the liquid surface always stays in the sixth bin. Accordingly, the temperature in the sixth bin from the Au surface is considered as the liquid surface temperature, T_L. To calculate the temperature, density, and molar flux in vapor, we evenly divide the central gas region into ten bins. The width of each bin in the central gas region is 10 nm. The molar flux in each bin is determined by $J_{MD} = = \Sigma v_{i,x}/(VN_A)$, where V is the volume of each bin in the central gas region, N_A is the Avogadro's number, and $v_{i,x}$ is the x-component of the velocity of vapor molecules within each bin. The contribution from macroscopic vapor velocity is subtracted in the calculation of vapor temperature in each bin. To determine the time dependence of molar flux, temperature, and density, we calculate the time-averaged J, T, and ρ in each bin every 108 ps. To improve the accuracy of the calculated properties, particularly the properties in the gas region, ten independent runs are carried out in each case. The uncertainties of the MD simulation results are determined by analyses of these independent runs.

With the aforementioned NEMD simulation method, one can readily obtain J, T_L, T_v, and ρ_v. To test the validity of Schrage relationships, i.e. Eqs. 1(a) and 1(b), one also needs to know the saturated vapor density, $\rho_g(T_L)$, and the MAC, $\alpha(T_L)$ of the model fluid Ar with a cutoff distance of 3.2σ. The saturated vapor density and the MAC of the model fluid Ar as a function of temperature have been determined by equilibrium MD (EMD) simulations in our previous work [9]. We will use the $\rho_g(T_L)$ and $\alpha(T_L)$ from our previous work in the theoretical analysis in this work.

2.3. Determination of thermal and mass diffusivity

To analyze thermal and mass transport in the model system in the course of the transient evaporation/condensation processes, we calculate the thermal diffusivity, D_{th}, and the mass diffusivity, D_M, of the saturated model fluid Ar at $T = 80$ K using EMD simulations. For the model fluid Ar at $T = 80$ K, the saturated pressure, P_{sat}, equals 0.68 atm and the density of the saturated liquid and saturated vapor is $\rho_f = = 34.8$ mol/L and $\rho_g = = 0.108$ mol/L, respectively [9]. We first carry out an EMD simulation in a cubic simulation box containing 4000 Ar atoms to determine D_{th} and D_M of the saturated vapor Ar. The side length of the cubic box is fixed at 39.48 nm such that the density of fluid equals to 0.108 mol/L. The Berendsen thermostat is used to equilibrate the system at $T = 80$ K for 3 ns. After the system reaches thermal equilibrium, we turn off the thermostat and run the simulation in a microcanonical ensemble. Mass diffusivity, D_M, is determined from the Green-Kubo formula [24]:

$$D_M = \frac{1}{3}\int_0^\infty \left\langle \vec{v}_i(t)\cdot\vec{v}_i(0)\right\rangle dt, \tag{4}$$

where $<\cdots>$ denotes the ensemble average, v_i is the velocity of atom i, and t is time. The thermal conductivity, k, of the fluid can be also determined from the Green-Kubo formula [24]:

$$k = \frac{V}{3k_BT^2}\int_0^\infty \left\langle \vec{q}(t)\vec{q}(0)\right\rangle dt, \tag{5}$$

where V is the volume of the simulation box and q is the microscopic heat flux which can be computed from [25,26]

$$\vec{q} = \frac{1}{V}\left[\sum_i E_i\vec{v}_i + \frac{1}{2}\sum_i\sum_j \vec{r}_{ij}\left(\vec{f}_{ij}\cdot\vec{v}_i\right)\right]. \tag{6}$$

In Eq. (6), E_i is the total energy of atom i, r_{ij} is the position vector from atom j to atom i, and f_{ij} is the interatomic force acting on atom i by atom j. To obtain good statistics of the simulation results, 1 μs is used to calculate the velocity autocorrelation function (VACF) in Eq. (4) and the heat flux autocorrelation function (HFACF) in Eq. (5). From the plateau of the running integral (see Fig. A1 in Appendix), we evaluate $D_M \approx 2.0 \times 10^{-6}$ m^2/s and $k \approx 0.0068$ W/m•K for the model saturated vapor Ar at $T = 80$ K. Using the ideal gas approximation for constant pressure specific heat, $c_p = = 2.5R_u$, for vapor Ar [27], where R_u is the universal gas constant, we obtain $D_{th} = = k/\rho c_p \approx 3.0 \times 10^{-6}$ m^2/s for the saturated vapor of the model fluid Ar at $T = 80$ K.

In a similar way, we evaluate D_{th} of the saturated liquid Ar. Using the EMD simulation and the Green-Kubo formula, we obtain $k \approx 0.12$ W/m•K for saturated liquid Ar at $T = 80$ K. This value is close to the experimental value of $k \approx 0.13$ W/m•K [28]. Furthermore, to evaluate the specific heat, c_p, of the saturated model liquid Ar at $T = 80$ K, we use the EMD simulation in a NPT ensemble to determine the enthalpy, h, of model liquid Ar at $T = 78$ K and $P = 0.68$ atm (i.e. P_{sat} at $T = 80$ K), and h at $T = 82$ K and $P = 0.68$ atm. The difference between the two h values divided by 4 K gives $c_p = = 45.5$ J/mol•K for the saturated liquid of the model fluid Ar at $T = 80$ K. The simulation result is close to the experimental value of 44.6 J/mol•K [28]. Using the k and c_p obtained from MD simulations, we obtain $D_{th} = = k/\rho c_p \approx 7.6 \times 10^{-8}$ m^2/s for the saturated liquid Ar at $T = 80$ K.

For further reference, we estimate the mean free path from the calculated mass diffusivity, D_M. Using the Einstein-Smoluchowski's equation [29,30], we find the mean free path of model Ar molecules in saturated vapor Ar at $T = 80$ K is about 19.4 nm. Accordingly, the Knudsen number of Ar in the vapor phase of the model system is ~0.2.

3. NEMD simulation results

3.1. Evaporation/condensation driven by a sudden temperature change

3.1.1. The driving force for the evaporation

In this case, the temperature of the left Au surface is suddenly changed to 90 K at $t = 0$ ps and maintained at 90 K in the rest of NEMD simulation. After the sudden rise of the temperature in the Au plate, the thermal energy propagates from the hot Au plate to the liquid on the Au plate by conduction. For heat conduction in liquid, the thermal transport speed is determined by D_{th} in the liquid. The left liquid surface is ~6 nm from the hot Au plate. According to the relation $L_{th} \approx 2\sqrt{D_{th}t}$, where L_{th} is the thermal diffusion length, it will take ~100 ps for the thermal energy to diffuse to the left liquid surface. As shown in Fig. 2, the temperature on the left liquid surface ($T_{L,1}$) indeed starts to increase at $t \approx 100$ ps, which is consistent with the above theoretical estimate. As the temperature at the liquid surface increases, the corresponding saturated vapor density increases and exceeds the density in the vapor near the liquid surface. As a result, the liquid on the hot surface evaporates, which leads to an increase of density in the vapor near the hot surface as shown in Fig. 3(c). The density gradient in the vapor phase then drives the mass flow from the left to right as shown in Fig. 1.

3.1.2. Heat and mass transfer mechanisms in vapor

After the evaporation starts at the left liquid surface, Fig. 1(b) shows that the mass flux, J, in the vapor phase keeps increasing with time, t, and decreasing with distance from the evaporating liquid in the first 3 ns of the NEMD simulation. After 3 ns, it is shown in Fig. 1(c) that J becomes essentially independent of t,

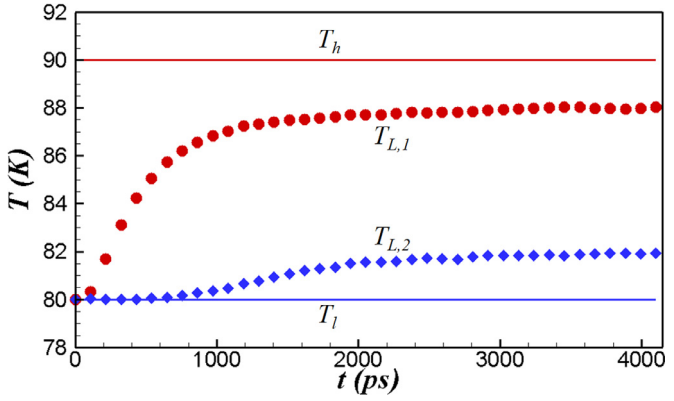

Fig. 2. The temperature of hot Au plate (Th), cold Au plate (Tl), hot liquid surface (TL,1), and cold liquid surface (TL,2) in the model system as a function of time. The results are obtained in the case when the evaporation and condensation are driven by a sudden increase of temperature in the left Au surface.

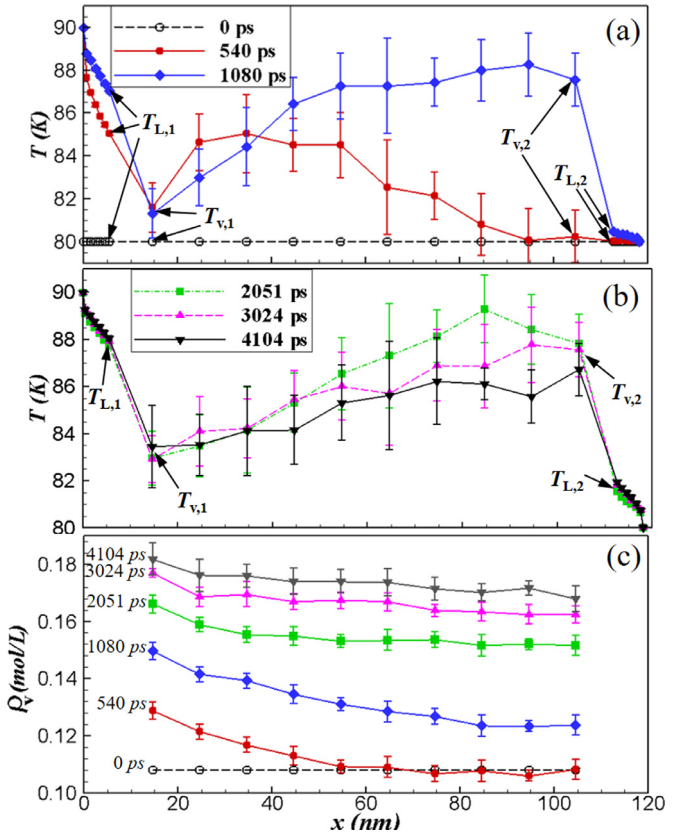

Fig. 3. The spatial distribution of temperature in the model system at (a) $t = 0$ ps, 540 ps, 1080 ps, and (b) $t = 2051$ ps, 3024 ps, and 4104 ps. (c) The spatial distribution of vapor density at $t = 0$ ps, 540 ps, 1080 ps, 2051 ps, 3024 ps, and 4104 ps. The evaporation and condensation are driven by a sudden increase of temperature in the left Au surface. TL,1 and TL,2 are the temperature at evaporating and condensing liquid surfaces, respectively. Tv,1 and Tv,2 are the vapor temperature in the bin closest to evaporating and condensing surfaces, respectively. The lines are used to guide the reader.

which indicates the model system reaches quasi-steady state evaporation and condensation. There are two possible heat and mass transfer mechanisms in the vapor phase. The first is convection, i.e. mass and energy transport by bulk fluid motion, and the second is conduction, i.e. heat and mass diffusion. To understand the heat and mass transfer mechanisms in the course of the transient evaporation and condensation processes, we analyze the temperature and density profiles obtained from MD simulations.

As shown in Fig. 3(a) and (c), at $t = 540$ ps the temperature of fluid less than 90 nm from the hot Au surface and the density of vapor less than 60 nm from the hot Au surface are affected by the hot surface on the left. The speed of heat and mass transfer by convection in the vapor phase is determined by the macroscopic speed of vapor. For $t < 540$ ps, the average macroscopic speed of vapor near the evaporating surface is ~20 m/s. Hence, the vapor molecules evaporated at $t \approx 100$ ps only travel a distance of ~9 nm at $t = 540$ ps. This travel distance is far less than the 90-nm thermal propagation distance and the 60-nm mass propagation distance found in Fig. 3(a) and (c).

To investigate if the transient heat and mass transfer in the vapor phase is mainly due to heat and mass diffusion at this stage, we calculate the thermal diffusion length ($L_{th} \approx 2\sqrt{D_{th}t}$) and the mass diffusion length ($L_M \approx 2\sqrt{D_M t}$). D_{th} and D_{M} both depend on the temperature. Fig. 3(a) shows the vapor temperature only varies between 80 K and 84 K in the first 540 ps. Within such a small temperature range, D_{th} and D_{M} only vary by several percent [27,28]. Hence, we can simply use a constant D_{th} and D_{M} evaluated at a temperature of 80 K to estimate L_{th} and L_{M} without causing a significant error. Since the evaporation starts at $t \approx 100$ ps, heat and mass have been transported in the vapor phase for 440 ps at $t = 540$ ps. Accordingly, we find $L_{th} \approx 74$ nm and $L_M \approx 60$ nm. Allowing for the initial diffusion distance of 6 nm in the liquid film in the first 100 ps, the total thermal and mass diffusion length at $t = 540$ ps are 80 nm and 66 nm, respectively. These values are consistent with those found in Fig. 3(a) and (c). Hence, our analysis shows the heat and mass transfer in the vapor phase is mainly due to the heat and mass diffusion in the vapor during transient evaporation and condensation in the nanochannel, rather than by convection. Of course, once the steady state starts to set in, convection becomes the main mass and energy transport mechanism.

Once the thermal energy from the hot surface diffuses to the cold liquid surface, the temperature at the right liquid surface starts to increase. The total length of the gas phase is ~100 nm. Using the relation $L_{th} \approx 2\sqrt{D_{th}t}$, we estimate that it takes ~830 ps for thermal energy to diffuse from the left liquid surface to the right liquid surface. Allowing for the initial heat diffusion in liquid film in the first 100 ps, thermal energy will arrive at the right liquid surface at $t \approx 930$ ps. As shown in Fig. 2, no evident increase in temperature at the right liquid surface ($T_{L,2}$) is found until $t \approx 900$ ps. This indicates that the delayed response of $T_{L,2}$ to the sudden temperature change in the left Au surface is mainly due to the thermal diffusion time in the vapor phase.

From the above analysis, we can see the heat and mass diffusion is the main heat and mass transfer mechanism in the vapor phase for the transient evaporation and condensation in a nanochannel. However, we expect the heat and mass convection will also be important for transient evaporation and condensation in macroscopic channels for larger times t, because the diffusion length is proportional to $\sqrt{t}$ and the propagation distance by convection (i.e. bulk fluid motion) is proportional to t. As the length of the vapor phase increases, the convection speed will eventually exceed the diffusion speed.

3.1.3. The density gradients in the vapor phase

In the course of transient evaporation and condensation in the model system, the density of vapor near the hot surface is always higher than that near the cold surface. As shown in Fig. 3(c), the density difference leads to mass diffusion, which makes the density gradient in the vapor phase gradually approach zero. When a quasi-steady state is reached ($t > 3$ ns), the density gradient in the vapor phase is close to zero and mass transfer by diffusion becomes negligible. At a quasi-steady state, the mass transfer from

the hot surface to the cold surface occurs by convection. The bulk fluid motion is mainly driven by the difference between the saturated vapor density $\rho_g(T_L)$ and the vapor density ρ_v near the evaporating and condensing interfaces. In this case, the main resistance to the mass transfer between two liquid surfaces is located at the two liquid-vapor interfaces rather than in the bulk vapor phase.

During quasi-steady state evaporation and condensation, the hot and cold liquid surfaces both move slowly towards the hot surface. As a result, $T_{L,1}$ and $T_{L,2}$ both increase slowly with time, but the difference between $T_{L,1}$ and $T_{L,2}$ is essentially a constant as shown in Fig. 2. Accordingly, the saturated vapor density $\rho_g(T_{L,1})$ and $\rho_g(T_{L,2})$ at the two interfaces also increase with time. That is why we see in Fig. 3(c) that the vapor density still increases slowly with time after the quasi-steady state is reached.

3.1.4. The temperature gradients in the vapor phase

The temperature profiles in the vapor phase at the early stage of the transient process (Fig. 3(a)) show several interesting characteristic. First, there is a temperature depression at the vapor next to the evaporating interface. This is caused by the fact that the evaporation process acts like a heat sink due to the thermal energy needed to break bonds between atoms in the liquid phase (heat of evaporation). Moreover, upon evaporation, a significant part of the thermal energy in vapor is converted to the macroscopic kinetic energy in the evaporating vapor flow. This reduces the vapor temperature near the evaporating interface. Analogously, once condensation starts at the liquid-vapor interface on the right side, the condensing interface acts as a heat source elevating the vapor temperature.

Second, in addition to the effect caused by the interfacial heat sources and sinks, there is a significant increase of the temperature inside the vapor phase (see Fig. 3(a)). To understand this behavior, we will analyze our results in terms to the continuum equation of the energy flow. Considering that from the macroscopic point of view, the simulated flow in our simulation is one-dimensional, we use the following equation of the compressible Newtonian fluids [31]:

$$\rho c_v \frac{\partial T}{\partial t} = -\rho c_v u \frac{\partial T}{\partial x} - P\frac{\partial u}{\partial x} + \mu \frac{4}{3}\left(\frac{\partial u}{\partial x}\right)^2 + k\frac{\partial^2 T}{\partial x^2} \quad (7)$$

The above equation expresses the rate of temperature change in terms of contributions from four physical processes: (i) energy advection due to mass flow, (ii) compression work, (iii) viscous dissipation, and (iv) diffusive heat conduction. Associated thermodynamic and transport parameters in the Eq. (7) include, u – flow velocity, T – temperature, P – pressure, ρ – density, μ - dynamics viscosity, and k – thermal conductivity. In our analysis, we will assume that the fluid is a monoatomic ideal gas, thus its internal energy can be expressed as c_vT, and $c_v = = 1.5R$ where R is the gas constant. Using a similar method to that described in Section 2.3 and the Green-Kubo formula for viscosity [32], we evaluate that the dynamic viscosity of saturated vapor Ar at a temperature of 80 K is ~6.5 μPa•s.

To estimate each of the four terms on the right-hand side of Eq. (7), we fitted the vapor temperature and velocity data (obtained by combining values from Figs. 1(b) and 3(c)) by 4th order polynomials to minimize the effects of statistical errors from MD simulations (see Fig. 4(a) and (b)). The vapor density data was fitted to a 3rd order polynomial as shown in Fig. 4(c). The order of the fitting polynomials was chosen such that it captures the essential trends in the data. Conclusions drawn from this continuum analysis remain unaltered when one order lower polynomial fits were used. It should be noted that higher order polynomials will overfit the data which undermines the sole purpose of fitting. Furthermore, our MD simulation results show the compressibility

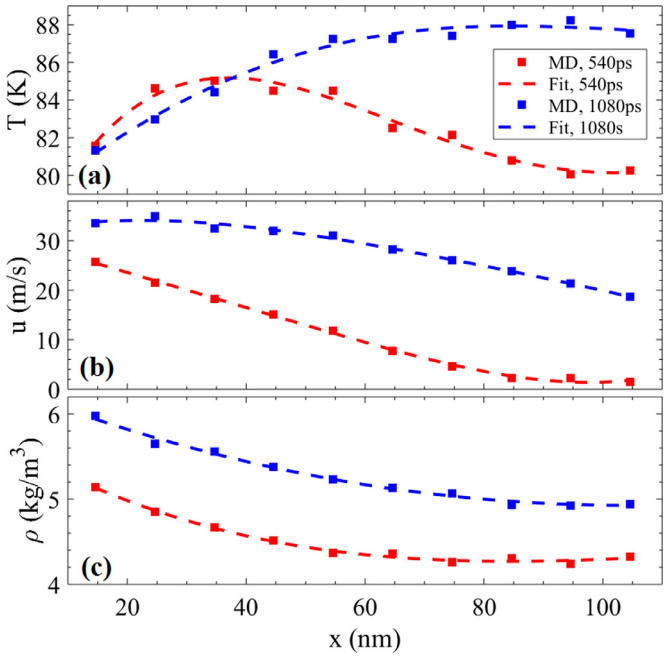

Fig. 4. The 4th order polynomial fit to MD data for (a) vapor temperature, and (b) vapor velocity. (c) The 3rd order polynomial fit to MD data for vapor density.

factor of the model vapor in the central vapor region is generally greater than 0.95. Therefore, the pressure in the vapor that is required to evaluate the compression work term is estimated using the ideal gas law.

The contributions to the rate of the temperature change from the four processes represented on the right-hand side of Eq. (7) for t = 540 ps and t = 1080 ps are shown in Fig. 5(a) and (b), respectively. For both time snapshots the term responsible for the temperature increase is mainly the compression work term. The other important term is the heat diffusion term that generally tends to decrease temperature. With the progress of the transient evaporation, the advection term also contributes to the temperature decrease inside the vapor. The viscous dissipation term is negligible for both cases. As the system reaches a quasi-steady state, the rate of temperature change due to the compression work decreases as the velocity gradient diminishes and thus the temperature profile flattens (see Fig. 3(b)).

However, due to the presence of the heat sink at the evaporating interface and the heat source the condensing interface, there is a persisting temperature gradient in the vapor between the lower temperature evaporating interface and the higher temperature condensing interface (see Fig. 3(b)). This temperature gradient in the vapor phase leads to heat conduction in the opposite direction of the mass flow in the vapor phase. Nevertheless, the net heat flux is still from the hot surface to the cold surface, since the magnitude of the heat conduction flux in the opposite direction is much smaller than the evaporation/condensation flux. Such an inverted temperature gradient in the vapor phase was also found in other MD studies of evaporation and condensation of LJ fluids [33,34] and in theoretical predictions [35].

3.1.5. Transient evaporation and condensation fluxes

In NEMD simulations, we divide the central gas region evenly into ten bins. The molar fluxes, J, determined in the leftmost and rightmost bins are considered as the evaporation flux (J_{evp}) and condensation flux (J_{con}), respectively. The J_{evp} and J_{con} obtained directly from MD simulations will be compared with the predictions from the Schrage relationships (i.e. Eq. (1)) to test the validity and

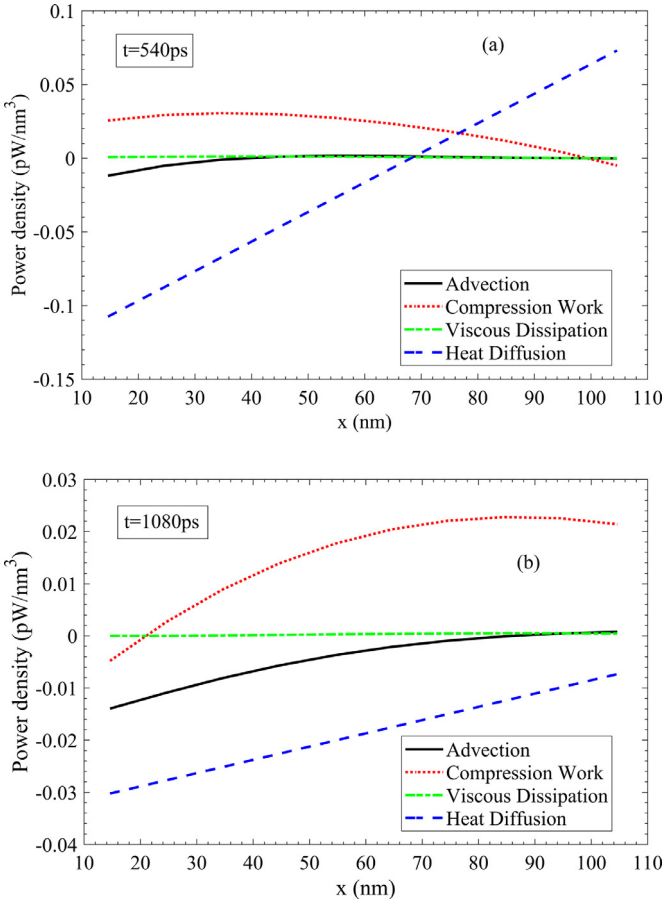

Fig. 5. Contributions to the rate of the temperature change in the vapor phase from the four terms in Eq. (7) at (a) 540 ps and (b) 1080 ps.

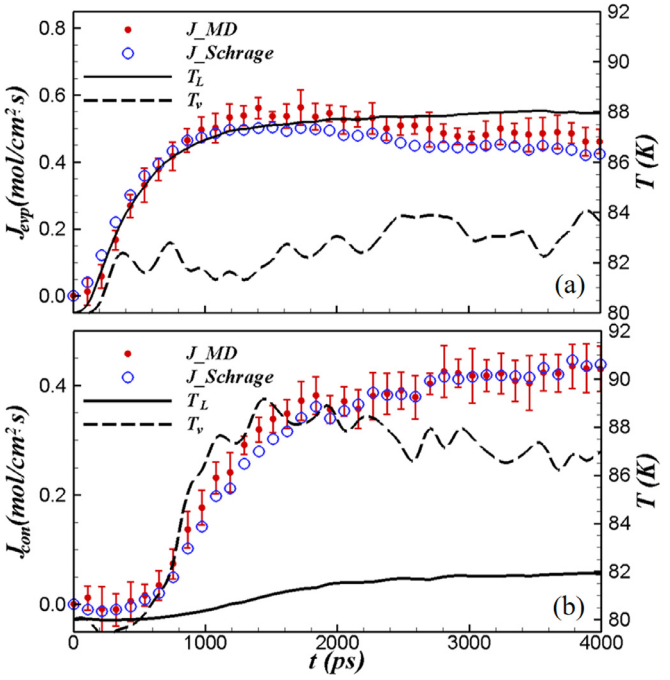

Fig. 6. (a) The evaporation molar flux, Jevp, and (b) the condensation molar flux, Jcon, as a function of time obtained from the NEMD simulation and the Schrage relationships. The temperature of liquid (TL) and vapor (Tv) near the (a) evaporating and (b) condensing interfaces are also shown. The results are obtained in the case when the evaporation and condensation are driven by a sudden increase of temperature in the left Au surface.

accuracy of the Schrage relationships in the prediction of the transient evaporation/condensation flux.

In Eq. (1), the liquid surface temperature T_L is obtained directly from MD simulations. The temperature and density of vapor (T_v and ρ_v) in Eq. (1) is the temperature and density of vapor near the evaporating and condensing surfaces. Therefore, in the calculation, we use the temperature and density in the leftmost and rightmost bins of the central gas region as T_v and ρ_v near the evaporating and the condensing surfaces, respectively. Furthermore, the saturated vapor density, $\rho_g(T_L)$, and the MAC, $\alpha(T_L)$, are obtained from the ρ_g vs. T and α vs. T data in our previous work [9].

With all this data, we obtain the theoretical prediction of transient evaporation and condensation fluxes. It is shown in Fig. 6 that the J_{evp} and J_{con} obtained directly from MD simulations agree with the predictions from the Schrage relationships very well. After the evaporation and condensation reach a quasi-steady state ($t > 3$ ns), we find $J_{evp} \approx J_{con} = = 0.45 \pm 0.04$ mol/cm^2•s. In our previous paper [9], we found $J_{evp} \approx J_{con} = = 0.46$ mol/cm^2•s for quasi-steady state evaporation and condensation in the case of $T_h = = 90$ K and $T_l = = 80$ K (i.e. case 2 in Table 1 of our previous paper [9]).

The evaporation on the left surface is initiated by the temperature increase in liquid. As shown Fig. 6(a), the increase of J_{evp} in the course of the transient evaporation process essentially follows the increase of temperature at the evaporating liquid surface (T_L). The condensation on the right surface is initiated by the arrival of the hot vapor molecules. Therefore, it is reasonable to see in Fig. 6(b) that the increase of J_{con} in the course of the transient condensation process essentially follows the increase of temperature in vapor (T_v) near the condensing surface.

3.1.6. The velocity distribution of vapor molecules

To provide further insight into the accuracy of the Schrage relationships in the prediction of transient evaporation and condensation fluxes, we note that a key assumption made in the derivation of Schrage relationships is that the vapor molecules adjacent to the evaporating/condensing interfaces have a Maxwell velocity distribution (VD) shifted by the mean velocity. In our previous work [9], we have shown that this assumption is accurate in the case of steady-state evaporation/condensation processes. To test if the assumption is also valid in the case of transient evaporation/condensation processes, we calculate the VD of vapor molecules in the leftmost (i.e. closest to the evaporating surface) and rightmost (i.e. closest to the condensing surface) bins of the central gas region every 108 ps. If the assumption made in Schrage's analysis is valid, the transient VD obtained directly from the MD simulation should follow the shifted Maxwell velocity distribution (SMVD) given by [8]

$$f(v_x) = \sqrt{\frac{m}{2\pi k_B T_v}} e^{-\frac{m\left(v_x - v_{v,0}\right)^2}{2k_B T_v}}, \tag{8}$$

where T_v and $v_{v,0}$ are the transient vapor temperature and the transient mean velocity of vapor molecules in each bin, respectively. Eq. (8) assumes the vapor temperature is isotropic. Near the evaporating and condensing surfaces, there is a Knudsen layer where the vapor temperature is anisotropic. In the course of transient evaporation and condensation processes studied in this work, the macroscopic velocity of vapor varies from 0 to ~ 30 m/s. Accordingly, $v_R = v_{v,0}/\sqrt{2k_B T_v/m}$ varies from 0 to ~0.16. When v_R is smaller than 0.16, our recent work [36] shows the extent of temperature anisopy in the Knudsen layer near the liquid surface is small, and the thickness of the Knudsen layer is only several nm for the model fluid. The central gas region in our model system is ~3 nm away from the liquid surface. This indicates the central gas region in our model system is essentially out of the region

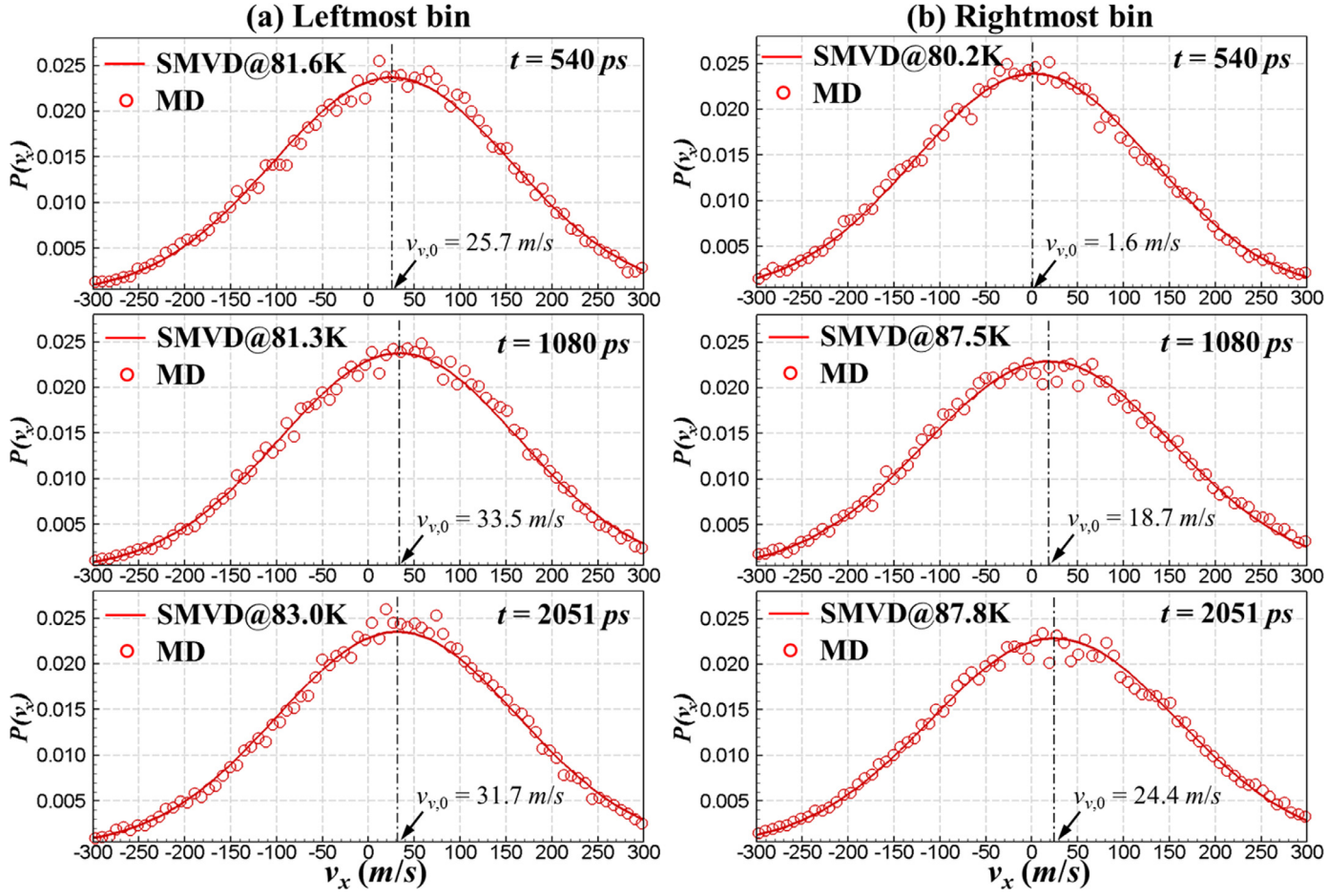

Fig. 7. The transient x-component VD of vapor molecules in the (a) leftmost bin (closet to the evaporating surface), and (b) rightmost bin (closest to the condensing surface) of the central gas region at t = 540 ps, 1080 ps and 2051 ps. The scatters are transient VDs obtained directly from MD simulations. The lines are the SMVD given by Eq. (8). The vertical dash-dot lines show the transient mean velocity of vapor molecules in each bin.

where temperature of vapor is significantly anisotropic. Hence, it is reasonable to consider the vapor in the central gas region as isotropic bulk vapor. In this case, if the VD of vapor molecules in the bin closest to the liquid surface still follows the SMVD given by Eq. (8) in the course of transient evaporation and condensation, the Schrage relationships should give good predictions of transient evaporation and condensation rates.

As shown in Fig. 7, the transient VDs obtained directly from MD simulation closely follow the SMVD given by Eq. (8). This indicates that establishing the SMVD near the liquid-vapor interface assumed by the Schrage analysis is a fast process relative to nanosecond time scales of the thermal relaxation processes in our study. This explains why the Schrage relationships are also accurate in the prediction of transient evaporation and condensation fluxes in our study.

3.2. Evaporation/condensation under an oscillatory driving force

3.2.1. The oscillatory driving force

In this section, we further study the evaporation and condensation under an oscillatory driving force. In this case, the temperature of the right Au plate is maintained at T_{l}= = 80 K, and the temperature of the left Au surface (T_{h}) changes between 80 K and 90 K as a sinusoidal function of time with an oscillatory period of 2 ns. All other settings are the same as those in the previous simulation. This study is motivated by the recent pulsed-laser based experimental work [18], which has the potential to allow studying frequency-dependent periodic heating of the solid surface that is in contact with an adsorbed nanoscopic liquid layer. The purpose of oscillatory temperature simulations is to test the response of evaporation-condensation process to an oscillatory driving force, and to see the validity of the Schrage equations in this limit.

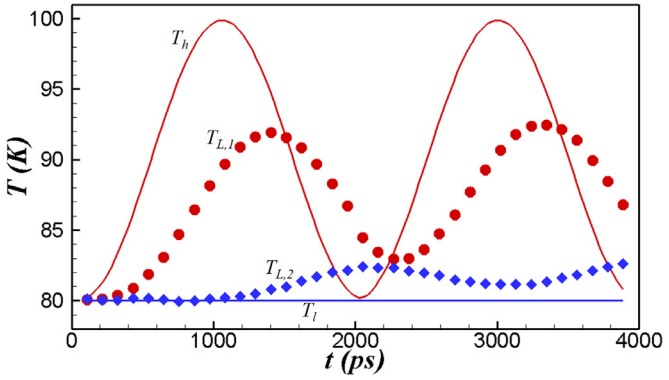

Fig. 8. The temperature of the hot Au plate (Th), cold Au plate (Tl), hot liquid surface (TL,1), and cold liquid surface (TL,2) in the model system as a function of time. The results are obtained in the case when Th varies as a sinusoidal function in the NEMD simulation.

As a consequence of oscillatory driving force, as shown in Fig. 8, the temperature at the evaporating and condensing liquid surfaces both oscillate with the same period as the driving force. Due to the thermal inertia in the liquid thin film, there is a phase difference

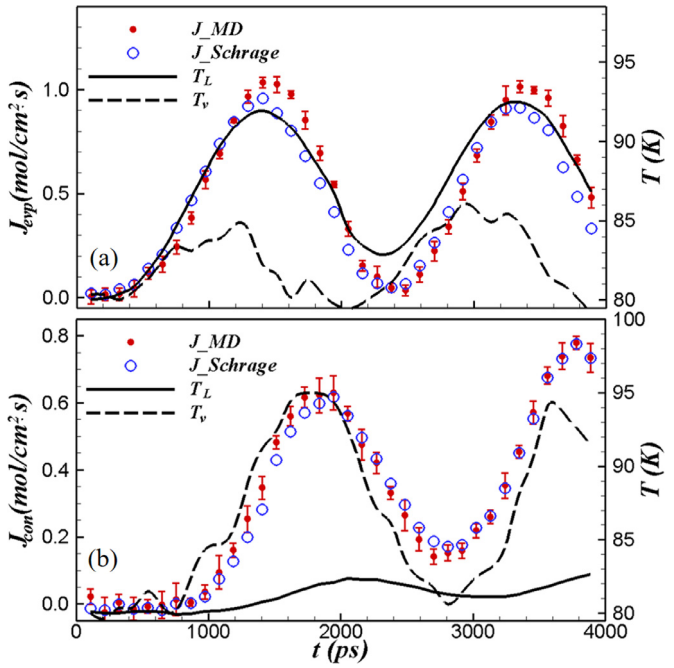

Fig. 9. (a) The evaporation molar flux, Jevp, and (b) the condensation molar flux, Jcon, as a function of time obtained from the NEMD simulation and the Schrage relationships. The temperature of liquid (TL) and vapor (Tv) near the (a) evaporating and (b) condensing interfaces is also shown. The results are obtained in the case when Th varies as a sinusoidal function in the NEMD simulation.

between oscillating T_h and $T_{L,1}$. As we discussed in Section 3.1.2, it takes ~800 ps for thermal energy to propagate from the left evaporating liquid surface to the right condensing liquid surface. This explains the 800 ps time difference between the peak of $T_{L,1}$ at the left liquid surface and the peak of $T_{L,2}$ at the right liquid surface shown in Fig. 8.

3.2.2. Transient evaporation and condensation fluxes

In Fig. 9 we compare J_{evp} and J_{con} obtained directly from NEMD simulations to those predicted from the Schrage relationships. The calculation process is similar to those described in Section 3.1.5. Fig. 9 shows that the Schrage relationships give good predictions of J_{evp} and J_{con} under the oscillatory driving force condition.

As shown in Fig. 9(a), the variation of J_{evp} essentially follows the change in T_L at the evaporating surface since the evaporation is mainly driven by the temperature variation of the liquid at the liquid-vapor interface. By contrast, the variation of J_{con} essentially follows the variation of T_v near the condensing surface (see Fig. 9(b)). These results are consistent with those found in Fig. 6(a) and (b).

4. Conclusions

Using MD simulations, we studied transient evaporation and condensation of fluid Ar in a nanochannel. The simulation results show that Schrage relationships are capable of accurately predicting transient evaporation and condensation fluxes even under an oscillatory driving force condition. The origin of this behavior is associated with the fact that establishing the velocity distribution near the liquid-vapor interface assumed by the Schrage analysis is a fast process relative to nanosecond time scales of the thermal relaxation processes in our study. Furthermore, our detailed analyses of the simulation results indicate that in the course of transient evaporation and condensation in a nanochannel, the heat and mass transfer in the vapor phase occurs mainly by heat and mass diffusion rather than by convection. This behavior is expected to always dominate at short time scales during pulse heating. However, at longer times relevant to evaporation/condensation processes in a macrochannel we expect that convection will also be important.

Author contribution statement

Z. L. conducted MD simulations and wrote the paper.

E. B. carried out MD simulations of properties of the model fluid.

A. C. conducted the continuum modeling in this work.

P. K. and Z. L. conceptualized the research, reviewed and edited the paper.

Acknowledgements

RPI authors (A. C. and P. K.) are grateful for the support provided by the Office of Naval Research Thermal Science Program, award #N00014-17-1-2767. CSU-Fresno authors (Z. L. and E. B.) would like to acknowledge the support of NSF CBET Thermal Transport Processes program under grant no. 1911433. Additionally, we would like to thank the eXtreme Science and Engineering Discovery Environment (XSEDE) for providing us supercomputer resources for MD simulations.

Supplementary materials

Supplementary material associated with this article can be found, in the online version, at doi:10.1016/j.ijheatmasstransfer.2019.119152.

Appendix

Fig. A1

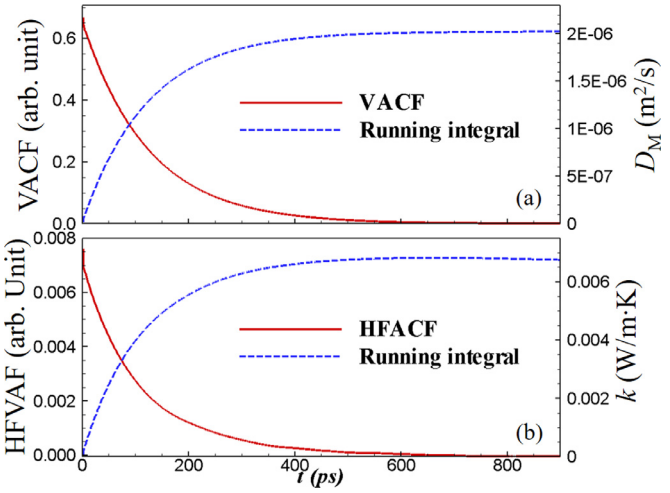

Fig. A1. (a) The VACF and its running integral, and (b) the HFACF and its running integral of the model saturated vapor Ar at a temperature of 80 K.

References

[1] A.H. Persad, C.A. Ward, Expressions for the Evaporation and Condensation Coefficients in the Hertz-Knudsen Relation, Chem. Rev. 116 (2016) 7727.
[2] M. Chaker, C.B. Meher-Homji, Gas turbine power augmentation: parametric study relating to Fog Droplet size and its influence on evaporative efficiency, J. Eng. Gas Turbines Power 133 (2011) 092001.
[3] R. Tao, K. Huang, H. Tang, D. Bell, Electrorheology leads to efficient combustion, Energy Fuels 22 (2008) 3785.
[4] T. Lim, S. Han, J. Chung, J.T. Chung, S. Ko, C.P. Grigoropoulos, Experimental study on spreading and evaporation of inkjet printed pico-liter droplet on a heated substrate, Int. J. Heat Mass Transfer 52 (2009) 431.

[5] J.-.U. Park, M. Hardy, S.J. Kang, K. Barton, K. Adair, D.K. Mukhopadhyay, C.Y. Lee, M.S. Strano, A.G. Alleyne, J.G. Georgiadis, P.M. Ferreira, J.A. Rogers, High-resolution electrohydrodynamic jet printing, Nat. Mat. 6 (2007) 782.
[6] H. Hertz, U. die, Verdunstung der Flüssigkeiten, insbesondere des Quecksilbers, im luftleeren Raume, Ann. Phys. 253 (1882) 177.
[7] M. Knudsen, Kinetic Theory of Gases, third ed., Methuene: London, London, 1950.
[8] R.W. Schrage, A Theoretical Study of Interphase Mass Transfer, Columbia University Press, New York, 1953.
[9] Z. Liang, T. Biben, P. Keblinski, Molecular simulation of steady-state evaporation and condensation: validity of the Schrage relationships, Int. J. Heat Mass Transf. 114 (2017) 105.
[10] Z. Liang, P. Keblinski, Molecular simulation of steady-state evaporation and condensation in the presence of a non-condensable gas, J. Chem. Phys. 148 (2018) 064708.
[11] J. Gonzalez, J. Ortega, Z. Liang, Prediction of thermal conductance at liquid-gas interfaces using molecular dynamics simulations, Int. J. Heat Mass Transf. 126 (2018) 1183.
[12] T. Ishiyama, T. Yano, S. Fujikawa, Molecular dynamics study of kinetic boundary condition at an interface between argon vapor and its condensed phase, Phys. Fluids 16 (2004) 2899–2906.
[13] T. Tsuruta, G. Nagayama, Molecular dynamics studies on the condensation coefficient of water, J. Phys. Chem. B 108 (2004) 1736–1743.
[14] B.-.Y. Cao, J.-.F. Xie, S.S. Sazhin, Molecular dynamics study on evaporation and condensation of n-dodecane at liquid-vapor phase equilibria, J. Chem. Phys. 134 (2011) 164309.
[15] J. Yu, H. Wang, A molecular dynamics investigation on evaporation of thin liquid films, Int. J. Heat Mass Transf. 55 (2012) 1218–1225.
[16] S. Shanthanu, S. Raghuram, V. Raghavan, Transient evaporation of moving water droplets in steam–hydrogen–air environment, Int. J. Heat Mass Transf. 64 (2013) 536.
[17] J. Kim, Spray cooling heat transfer: the state of the art", Int. J. Heat Fluid Flow 28 (2007) 753.
[18] J. Park, X. Xie, D. Li, D.G. Cahill, Plasmonic sensing of ultrafast evaporation and condensation, Nano. Micro. Therm. Eng. 21 (2017) 70.
[19] S.M. Foiles, M.I. Baskes, M.S. Daw, Embedded-atom-method functions for the fcc metals Cu, Ag, Au, Ni, Pd, Pt, and their alloys, Phys. Rev. B 33 (1986) 7983.
[20] G.C. Maitland, M. Rigby, E.B. Smith, W.A. Wakeham, Intermolecular Forces: Their Origin and Determination, Clarendon Press, Oxford, 1981.
[21] D. Frenkel, B. Smit, Understanding Molecular Simulation, Academic Press, San Diego, 2002.
[22] H.J.C. Berendsen, J.P.M. Postma, W.F. Van Gunsteren, A. Di Nola, J.R. Haak, Molecular dynamics with coupling to an external bath, J. Chem. Phys. 81 (1984) 3684.
[23] P. Jund, R. Jullien, Molecular-dynamics calculation of the thermal conductivity of vitreous silica, Phys. Rev. B 59 (1999) 13707.
[24] D. Frenkel, B. Smit, in: Understanding Molecular Simulation, Academic Press, San Diego, 2002, p. 75.
[25] S. Srinivasan, R.S. Miller, On Parallel Nonequilibrium Molecular Dynamics Simulations of Heat Conduction in Heterogeneous Materials with Three-Body Potentials: Si/Ge Superlattice, Num. Heat Transf. Part B 52 (2007) 297.
[26] Y. Chen, Stochastic Problems in Physics and Astronomy, J. Chem. Phys. 124 (2006) 054113.
[27] Y.A. Çengel, M.A. Boles, Thermodynamics – An Engineering Approach, eighth ed., McGraw Hill Education, New York, 2015.
[28] E.W. Lemmon, M.O. McLinden, D.G. Friend, Thermophysical properties of fluid systems, in: P.J. Linstrom, W.G. Mallard (Eds.), NIST Chemistry WebBook, NIST Standard Reference Database Number 69, National Institute of Standards and Technology, Gaithersburg, MD, USA, 2003.
[29] S. Chandrasekhar, Stochastic Problems in Physics and Astronomy, Rev. Mod. Phys 15 (1943) 20.
[30] F.O. Goodman, H.Y. Wachman, Dynamics of Gas-Surface Scattering, Academic, New York, 1976.
[31] M. E.Gurtin, E. Fried, L. Anand, The Mechanics and Thermodynamics of Continua, Cambridge University Press, 2010.
[32] Z. Liang, H.-L. Tsai, Prediction of the Transport Properties of a Polyatomic Gas, Fluid Phase Equilib. 293 (2010) 196.
[33] R. Meland, Molecular dynamics simulation of the inverted temperature gradient phenomenon, Phys. Fluids 15 (2003) 3244.
[34] O. Wilhelmsen, T.T. Trinh, A. Lerik, Temperature anisotropy at equilibrium reveals nonlocal entropic contributions to interfacial properties, Phys. Rev. E 97 (2018) 012126.
[35] Y.-P. Pao, Application of Kinetic Theory to the Problem of Evaporation and Condensation, Phys. Fluids 14 (1971) 306.
[36] E. Bird, Z. Liang, Transport phenomena in the Knudsen layer near an evaporating surface, Phys. Rev. E 100 (2019) 043108.